Monthly Notices of the ROYAL ASTRONOMICAL SOCIETY

MNRAS **500,** 4126–4138 (2021) doi:10.1093/mnras/staa3462
Advance Access publication 2020 November 7

Disc fragmentation and intermittent accretion on to supermassive stars

Ryoki Matsukoba,[1★] Eduard I. Vorobyov,[2,3] Kazuyuki Sugimura ,[1,4] Sunmyon Chon,[1]
Takashi Hosokawa[5] and Kazuyuki Omukai[1]

[1]*Astronomical Institute, Graduate School of Science, Tohoku University, Aoba, Sendai, Miyagi 980-8578, Japan*
[2]*Department of Astrophysics, University of Vienna, Vienna 1180, Austria*
[3]*Ural Federal University, 51 Lenin Str., 620051 Ekaterinburg, Russia*
[4]*Department of Astronomy, University of Maryland, College Park, MD 20740, USA*
[5]*Department of Physics, Graduate School of Science, Kyoto University, Sakyo, Kyoto 606-8502, Japan*

Accepted 2020 November 3. Received 2020 October 19; in original form 2020 September 17

ABSTRACT

Supermassive stars (SMSs) with $\sim 10^4$–10^5 $M_\odot$ are candidate objects for the origin of supermassive black holes observed at redshift $z > 6$. They are supposed to form in primordial-gas clouds that provide the central stars with gas at a high accretion rate, but their growth may be terminated in the middle due to the stellar ionizing radiation if the accretion is intermittent and its quiescent periods are longer than the Kelvin–Helmholtz (KH) time-scales at the stellar surfaces. In this paper, we examine the role of the ionizing radiation feedback based on the accretion history in two possible SMS-forming clouds extracted from cosmological simulations, following their evolution with vertically integrated two-dimensional hydrodynamic simulations with detailed thermal and chemical models. The consistent treatment of the gas thermal evolution is crucial for obtaining the realistic accretion history, as we demonstrate by performing an additional run with a barotropic equation of state, in which the fluctuation of the accretion rate is artificially suppressed. We find that although the accretion becomes intermittent due to the formation of spiral arms and clumps in gravitationally unstable discs, the quiescent periods are always shorter than the KH time-scales, implying that SMSs can form without affected by the ionizing radiation.

Key words: accretion, accretion discs – cosmology: theory – dark ages, reionization, first stars.

1 INTRODUCTION

More than 200 supermassive black holes (SMBHs) with 10^7–10^{10} $M_\odot$ at redshift $z > 6$ have been discovered by recent observations of high-redshift quasars (e.g. Venemans et al. 2013; Bañados et al. 2018; Matsuoka et al. 2018; Onoue et al. 2019; see also Gallerani et al. 2017, for a review). Although the standard formation scenario explaining the origin of these BHs has not yet been established, massive seed BHs are preferred because the existence of the high-redshift SMBHs suggests that they have to grow to SMBHs in a short time (see, e.g. Volonteri 2012; Haiman 2013; G29,; Inayoshi, Visbal & Haiman 2019 for a review).

Remnant BHs of Pop III stars have been considered as candidates of seed BHs by some authors (e.g. Madau & Rees 2001). They possibly grow to the observed high-redshift SMBHs, either by continuous accretion at Eddington limit or by short episodic accretion at a super-Eddington rate. In practice, however, it is hard to realize such accretion growths because accretion flows on to seed BHs are easily inhibited by their own radiation together with the gas angular momentum (Milosavljević, Couch & Bromm 2009; Park & Ricotti 2011; Sugimura et al. 2018; but see also Inayoshi, Haiman & Ostriker 2016; Sugimura et al. 2017).

An alternative SMBH formation channel is the so-called direct collapse scenario (e.g. Bromm & Loeb 2003), in which supermassive stars (SMSs) with $\sim 10^4$–10^5 $M_\odot$ collapse into seed BHs with the similar mass after their lifetime (Umeda et al. 2016). The SMSs are supposed to form in primordial-gas clouds if the clouds collapse almost isothermally at $\sim 10^4$ K due to the atomic hydrogen cooling, with the formation of molecular hydrogen fully suppressed by strong external far-ultraviolet (UV) radiation from nearby galaxies (Omukai 2001; Shang, Bryan & Haiman 2010; Regan, Johansson & Wise 2014; Sugimura, Omukai & Inoue 2014). The high gas temperature of the clouds leads to a high accretion rate of 0.1–1 $M_\odot$ yr^{-1} on to the protostars formed at the centre (Latif et al. 2013; Inayoshi, Omukai & Tasker 2014; Becerra et al. 2015), as well as prevents the vigorous gas fragmentation in the clouds. Due to the high accretion rate, the surface of protostars substantially inflates and the effective temperature drops to several 1000 K (Hosokawa, Omukai & Yorke 2012; Hosokawa et al. 2013). As a result, the accretion flow continues without affected by the radiative feedback, allowing the protostars to reach the mass of $\sim 10^4$–10^5 $M_\odot$ within their short lifetime (∼Myr).

In order to maintain the inflated stellar surface with a constant accretion rate, the accretion rate must be higher than the critical value of 4×10^{-2} $M_\odot$ yr^{-1}, as shown in Omukai & Palla (2003) and Hosokawa et al. (2012, 2013) (but see Haemmerlé et al. 2018a for discussion that the critical value decreases below 10^{-2} $M_\odot$ yr^{-1} if the stellar mass is above 600 $M_\odot$). If the accretion rate temporarily drops below the critical value for sometime, the stellar surface

★ E-mail: r.matsukoba@astr.tohoku.ac.jp

begins to shrink, and hence the effective temperature rises. The ionizing radiation from the shrinking protostar may quench the accretion before acquiring enough mass to reach the SMS regime. By performing stellar evolution calculations with an accretion model with repeating burst and quiescent phases, Sakurai et al. (2015) showed that ionizing radiation from the protostar becomes strong enough to significantly suppress the accretion if a quiescent period of the intermittent accretion $\Delta t_{\rm q}$, which is defined as the time duration for which the accretion rate is below the critical value, is longer than the Kelvin–Helmholtz (KH) time-scale at the stellar surface,

$$t_{\rm KH,surf} = 10^3\ {\rm yr}\ \left(\frac{M_*}{500\ M_\odot}\right)^{1/2}. \quad (1)$$

The time variation of the accretion rate can be caused by the fragmentation of the circumstellar discs due to the gravitational instability, as suggested in the stability analysis of the discs around growing SMSs (Inayoshi & Haiman 2014; Latif & Schleicher 2015; Matsukoba et al. 2019). Sakurai et al. (2016) confirmed that the disc fragmentation due to the gravitational instability in fact causes the fluctuation of the accretion rate, by performing vertically integrated two-dimensional simulations of the discs around growing SMSs. From the stellar evolution calculations with the accretion rate obtained from the simulations, they also concluded that SMSs can grow by accretion without affected by the radiative feedback. Consistently, the quiescent periods observed in their simulations were always shorter than the KH time-scale given in equation (1).

Their simulations, however, adopted a barotropic equation of state to model the thermal evolution of gas, instead of solving the energy equation. Considering that the temperature of the gas plays a critical role in determining the gravitational stability of the discs, this approximation may affect their conclusion on the role of radiative feedback. Most importantly, their barotropic relation was an inadequate approximation because it is based on the thermal evolution of collapsing cores (Omukai 2001), which is largely different from that of discs (Matsukoba et al. 2019). Therefore, in this paper, we perform simulations of SMS formation considering detailed thermal and chemical processes and re-examine whether the protostars can grow to SMSs without affected by the radiative feedback.

This paper is organized as follows. We describe our simulation model and the initial conditions in Section 2. We then present the time evolution of disc structures and central stars, as well as the comparison with a simulation with a barotropic relation, in Section 3. Summary and discussion are given in Section 4.

2 METHOD

We follow the time evolution of the discs around growing SMSs using vertically integrated two-dimensional simulations with a detailed treatment of chemical and thermal processes. Here, we first briefly explain the method for the hydrodynamic simulations and then describe the thermal processes, chemical reactions, and initial conditions adopted in this study. The details of the hydrodynamic method are described in Vorobyov et al. (2020).

2.1 Hydrodynamic simulations

Here, we describe the method for our vertically integrated two-dimensional simulations used to follow the gas dynamics around growing SMSs. We use polar-coordinate $(r,\ \phi)$ grids with 512×512 spatial zones. The computational domain extends to the outer radius of $r_{\rm out} = 2 \times 10^6$ au, with the sink cell with the size $r_{\rm sc} = 300$ au introduced at the centre. At each time-step, we measure the mass flowing into the sink cell, in which we assume that a central star is surrounded by an unresolved disc, and increase the stellar mass according to the following sink-cell model: 4 per cent of the gas flowing into the sink cell is deposited in the unresolved disc, 9.6 per cent is carried away by the stellar jet, and the rest accretes on to the central star. We initially set the stellar mass to zero and the surface density of the sink cell to the same as in the innermost grids.

To follow the hydrodynamic evolution of the gas, we solve the vertically integrated mass, momentum, and energy transport equations:

$$\frac{\partial \Sigma}{\partial t} = -\nabla_{\rm p} \cdot \left(\Sigma \boldsymbol{u}_{\rm p}\right), \quad (2)$$

$$\frac{\partial}{\partial t}\left(\Sigma \boldsymbol{u}_{\rm p}\right) + \left[\nabla \cdot \left(\Sigma \boldsymbol{u}_{\rm p} \otimes \boldsymbol{u}_{\rm p}\right)\right]_{\rm p} = -\nabla_{\rm p} P + \Sigma \boldsymbol{g}_{\rm p} + (\nabla \cdot \boldsymbol{\Pi})_{\rm p}, \quad (3)$$

$$\frac{\partial e}{\partial t} + \nabla_{\rm p} \cdot \left(e \boldsymbol{u}_{\rm p}\right) = -P\left(\nabla_{\rm p} \cdot \boldsymbol{u}_{\rm p}\right) - Q_{\rm net} + (\nabla \boldsymbol{u})_{\rm pp'} : \boldsymbol{\Pi}_{\rm pp'}, \quad (4)$$

where the subscripts p and p' represent the planar components $(r,\ \phi)$ in the polar coordinates, Σ is the surface density, $\boldsymbol{u}_{\rm p} = u_{\rm r}\hat{\boldsymbol{r}} + u_\phi \hat{\boldsymbol{\phi}}$ is the planar velocity, P is the vertically integrated gas pressure, $\nabla = \hat{\boldsymbol{r}}\partial/\partial r + \hat{\boldsymbol{\phi}} r^{-1}\partial/\partial\phi$ is the gradient in the disc plane, $\boldsymbol{g}_{\rm p} = g_{\rm r}\hat{\boldsymbol{r}} + g_\phi\hat{\boldsymbol{\phi}}$ is the gravitational acceleration including the gravity of the central star and the self-gravity of the circumstellar disc, e is the internal energy per unit area, and $Q_{\rm net}$ is the net cooling rate per unit area, which we describe in Section 2.2. The gas pressure and internal energy are related by the ideal-gas equation of state,

$$P = (\gamma - 1)e, \quad (5)$$

with the adiabatic exponent γ, which we consistently calculate according to the chemical composition considering the rotational and vibrational degrees of freedom of the H_2. The gas mass density and temperature, which are used for the computation of the thermal and chemical evolution, are given, respectively, by

$$\rho = \frac{\Sigma}{\sqrt{2\pi}\, H_{\rm g}} \quad (6)$$

and

$$T = (\gamma - 1)\frac{\mu m_{\rm H}}{k_{\rm B}}\frac{e}{\Sigma}, \quad (7)$$

where $H_{\rm g}$ is the gas scale height estimated from the vertical hydrostatic balance in the gravitational fields of the star and disc (see Vorobyov & Basu 2009), μ is the mean molecular weight, $k_{\rm B}$ is the Boltzmann constant, and $m_{\rm H}$ is the mass of a hydrogen nucleus. The self-gravity of the disc is computed by taking the gradient of the gravitational potential

$$\Phi(r,\ \phi) = -G \int_{r_{\rm sc}}^{r_{\rm out}} r' {\rm d}r' \times \int_0^{2\pi} \frac{\Sigma(r',\ \phi')}{\sqrt{r'^2 + r^2 - 2rr'\cos(\phi' - \phi)}}\,{\rm d}\phi'. \quad (8)$$

The turbulent viscosity is considered with the viscous stress tensor,

$$\boldsymbol{\Pi} = 2\Sigma\nu\left(\nabla \boldsymbol{u} - \frac{1}{3}(\nabla \cdot \boldsymbol{u})\boldsymbol{e}\right), \quad (9)$$

where $\boldsymbol{e}$ is the unit tensor and ν is the kinematic viscosity, which is given according to the α-viscosity prescription (Shakura & Sunyaev 1973),

$$\nu = \alpha c_{\rm s} H_{\rm g}. \quad (10)$$

Here, $c_s = \sqrt{\gamma P/\Sigma}$ is the sound velocity. In this study, we set $\alpha = 10^{-4}$. Although we consider the angular momentum transport due to the turbulent viscosity, the primary angular momentum transport mechanism is that due to the gravitational torque.

2.2 Thermal processes

The net cooling rate per unit area is given by

$$Q_{\rm net} = \int \Lambda_{\rm net}\, {\rm d}z = 2H_{\rm g}\Lambda_{\rm net}, \tag{11}$$

where $\Lambda_{\rm net}$ is the net cooling rate per unit volume. The value of $\Lambda_{\rm net}$ is the sum of the rates of H_2-line cooling Λ_{H_2}, Ly α cooling $\Lambda_{{\rm Ly}\,\alpha}$, continuum cooling $\Lambda_{\rm cont}$, chemical cooling $\Lambda_{\rm chem}$, H^- photodetachment heating $\Gamma_{\rm PD}$, and stellar irradiation heating $\Gamma_{\rm irr}$:

$$\Lambda_{\rm net} = \Lambda_{H_2} + \Lambda_{\rm cont} + \Lambda_{{\rm Ly}\alpha} + \Lambda_{\rm chem} - \Gamma_{\rm PD} - \Gamma_{\rm irr}. \tag{12}$$

The H_2-line cooling rate is given by

$$\Lambda_{H_2} = \overline{\beta}_{{\rm esc},H_2}\Lambda_{H_2,{\rm thin}}{\rm e}^{-\tau}, \tag{13}$$

where $\Lambda_{H_2,{\rm thin}}$ is the optically-thin rate (Glover 2015), $\overline{\beta}_{{\rm esc},H_2}$ is the line-averaged escape probability (Fukushima, Omukai & Hosokawa 2018), and τ is the effective optical depth for continuum radiation. The effective optical depth

$$\tau = \sqrt{\tau_{\rm P}\tau_{\rm R}}, \tag{14}$$

is calculated with the Planck (Rosseland) mean optical depth,

$$\tau_{\rm P(R)} = \frac{1}{2}\Sigma\,\kappa_{\rm P(R)}, \tag{15}$$

for which we use the Planck (Rosseland) mean opacity $\kappa_{\rm P(R)}$ provided by Mayer & Duschl (2005). Similarly, the Ly α cooling rate is given by

$$\Lambda_{{\rm Ly}\,\alpha} = \overline{\beta}_{{\rm esc,Ly}\,\alpha}\Lambda_{{\rm Ly}\,\alpha,{\rm thin}}{\rm e}^{-\tau}, \tag{16}$$

where $\Lambda_{{\rm Ly}\,\alpha,\,{\rm thin}}$ is optically-thin rate (Cen 1992) and $\overline{\beta}_{{\rm esc,Ly}\,\alpha}$ is the escape probability estimated by using the method in Inayoshi et al. (2016). We consider H free–bound emission, H^- free–bound emission, H^- free–free emission, H free–free emission, H_2-H_2 collision-induced emission, and H_2-He collision-induced emission as the continuum radiation processes. The H^- free–bound emission plays the primary role as a coolant in the circumstellar discs (Matsukoba et al. 2019). We use the fitting formula for the continuum cooling rate in the optically thin regime $\Lambda_{\rm cont,\,thin}$ from Matsukoba et al. (2019) and smoothly connect the rates in the optically thin and thick limits (Becerra et al. 2018):

$$\Lambda_{\rm cont} = \Lambda_{\rm cont,thin}\left(1 + \frac{3}{2}\tau^2\right)^{-1}. \tag{17}$$

The chemical cooling/heating processes include H ionization/recombination, H_2 dissociation/formation, and H^- detachment/attachment. The chemical cooling rate is calculated as follows:

$$\Lambda_{\rm chem} = \left(\frac{{\rm d}y(H^+)}{{\rm d}t}\chi_{\rm H} - \frac{{\rm d}y(H_2)}{{\rm d}t}\chi_{H_2} - \frac{{\rm d}y(H^-)}{{\rm d}t}\chi_{H^-}\right)n_{\rm H}, \tag{18}$$

where $\chi_{\rm H}$=13.6, χ_{H_2}=4.48, and χ_{H^-}=0.755 eV are the binding energies. The chemical fraction of species i, $y(i)$, is defined by the ratio of its number density $n(i)$ and that of hydrogen nuclei $n_{\rm H}$:

$$y(i) = \frac{n(i)}{n_{\rm H}}. \tag{19}$$

The number density of hydrogen nuclei is given by

$$n_{\rm H} = \frac{\rho}{(1+4y_{\rm He})\,m_{\rm H}}, \tag{20}$$

where $y_{\rm He}$ is the fractional abundance of helium.

In SMS formation, H^- photodetachment by external radiation may contribute to the suppression of H_2 formation in the low-density region. The gas is also heated upon photodetachment because the excess photon energy is stored as the kinetic energy of photodetached free electrons. The H^- photodetachment heating rate is given by

$$\Gamma_{\rm PD} = \epsilon_{\rm PD}\, n_{\rm H}\, y(H^-)\, k_{22}, \tag{21}$$

where $\epsilon_{\rm PD}$ is the average heating rate per reaction, and k_{22} is the photodetachment rate per H^- ion (reaction number 22 in Table A1). The average heating rate per reaction is calculated as

$$\epsilon_{\rm PD} = \frac{\int 4\pi\frac{J_{\rm ex}(\nu)}{h\nu}\sigma_{\rm PD}(\nu)h\nu\,{\rm d}\nu}{\int 4\pi\frac{J_{\rm ex}(\nu)}{h\nu}\sigma_{\rm PD}(\nu)\,{\rm d}\nu}, \tag{22}$$

with the reaction cross-section $\sigma_{\rm PD}$ (John 1988) and the external radiation intensity $J_{\rm ex}(\nu)$. As in Chon, Hosokawa & Yoshida (2018), we simply assume the blackbody radiation spectrum,

$$J_{\rm ex}(\nu) = 10^{-21}J_{21} \times \frac{B_\nu(T_{\rm ex})}{B_{13.6\,{\rm eV}}(T_{\rm ex})}{\rm e}^{-\tau}\ {\rm erg\ s^{-1}\ Hz^{-1}\ str^{-1}\ cm^{-2}}, \tag{23}$$

with the Planck function $B_\nu(T_{\rm ex})$ and the far-UV intensity J_{21} (in the unit of 10^{-21} erg s^{-1} Hz^{-1} str^{-1} cm^{-2} at $h\nu = 13.6$ eV), and set the radiation temperature $T_{\rm ex} = 10^4$ K (but see also Sugimura et al. 2014, for discussion about realistic radiation spectra). This yields $\epsilon_{\rm PD} =$ 2.23 eV, independently of τ and J_{21},

Our thermal model also takes into account the central stellar irradiation heating. As the star grows and its luminosity increases, it may affect the gas temperature. The stellar irradiation heating rate is calculated as

$$\Gamma_{\rm irr} = \frac{4\sigma_{\rm SB}\rho}{1+\frac{3}{2}\tau^2}\kappa_{\rm P}(T_{\rm irr})T_{\rm irr}^4, \tag{24}$$

with the Stefan–Boltzmann constant $\sigma_{\rm SB}$ and the irradiation temperature $T_{\rm irr}$, which is given by

$$T_{\rm irr} = \left(G(\tau)\frac{L_*}{4\pi\sigma_{\rm SB}r^2}\right)^{1/4}. \tag{25}$$

The function $G(\tau)$ smoothly connects the values in both the optically thin and thick regimes:

$$G(\tau) = \frac{1}{4} + \frac{2}{\pi}\left(\cos\gamma_{\rm irr} - \frac{1}{4}\right)\arctan(\tau), \tag{26}$$

with the incident angle of stellar irradiation to the disc $\gamma_{\rm irr}$ (Vorobyov & Basu 2010). This function becomes 1/4 in the optically thin regime and $\cos\gamma_{\rm irr}$ in the optically thick regime. We compute the stellar luminosity L_* using the analytical formula obtained from stellar evolution calculations (Hosokawa et al. 2012):

$$L_* = 3.8\times10^6\,L_\odot\left(\frac{M_*}{100\,M_\odot}\right), \tag{27}$$

where M_* is the stellar mass.

It is known that artificial fragmentation occurs in hydrodynamic simulations if the Jeans length $\lambda_{\rm J}$ becomes less than four times the grid size $x_{\rm grid}$ (Truelove et al. 1997). In order to prevent such artificial fragmentation, we cut off the cooling by introducing a suppression factor (Hosokawa et al. 2016),

Table 1. Initial properties of the simulated clouds.

	r_c (pc)	M_c ($M_\odot$)	M_{tot} ($M_\odot$)	Ω_c (s^{-1})	J_{21}	T (K)	y(H$_2$)	y(H$^+$), y(e)
Filamentary	1.35	5.5×10^4	7.9×10^5	5.8×10^{-14}	5000	7100	1.8×10^{-9}	7.3×10^{-5}
Spherical	1.47	5.6×10^4	6.8×10^5	2.8×10^{-14}	1000	7100	1.8×10^{-9}	7.3×10^{-5}

Note. The parameters from the left to right correspond to the core radius, core mass, total mass, core angular velocity, far-UV intensity, temperature, and chemical fractions of H$_2$, H$^+$, and e.

$$C_{\rm limit} = \exp\left[-\left(\frac{\xi - 1}{0.1}\right)^2\right], \tag{28}$$

$$\xi = f_{\rm limit}\frac{x_{\rm grid}}{\lambda_{\rm J}}, \tag{29}$$

and multiplying $\Lambda_{\rm net}$ by this factor. We set $f_{\rm limit} = 6$ in our model, and hence the cooling is suppressed when $\lambda_{\rm J}$ becomes less than six times $x_{\rm grid}$.

For comparison with the previous study (Sakurai et al. 2016), we also perform hydrodynamic simulations using the barotropic temperature–density relation described in Appendix B, instead of solving the energy equation (equation 4). We describe the results from the simulations with the barotropic relation in Section 3.3.

2.3 Chemical reactions

We follow the chemical evolution of the primordial gas, solving the chemical network of five species, H, H$_2$, H$^+$, H$^-$, and e, and 22 reactions, summarized in Table A1. Our chemical network was selected so as to correctly follow the thermal evolution of both collapsing clouds and circumstellar discs in the SMS formation (Omukai 2001; Matsukoba et al. 2019). In our chemical model, we solve the non-equilibrium kinetic equations for H, H$_2$, H$^+$, and e, with H$^-$ assumed to be in the chemical equilibrium of all related reactions. We assume that all helium is neutral, with the fractional abundance $y_{\rm He} = 8.333 \times 10^{-2}$. We further solve the continuity equation for each species assuming the collisional coupling with the gas.

2.4 Initial conditions

We start our simulations from the initial conditions extracted from the previous cosmological simulations in Chon et al. (2016) and follow the SMS formation from the pre-stellar core stage until the masses of the central stars reach 30 000 $M_\odot$. Chon et al. (2016) performed tens of zoom-in hydrodynamic simulations in a parent volume of 30 Mpc on a side and identified two collapsing primordial gas clouds that are exposed by strong far-UV radiation from nearby galaxies and possibly form SMSs later on. We extract these two clouds, which were labelled *filamentary* and *spherical* clouds from their shapes, when the core density reaches 10^5 cm^{-3}.

The properties of the two clouds are summarized in Table 1. The two clouds have almost the same mass, but the angular velocity of the core is larger in the *filamentary* cloud. For each cloud, we set our initial conditions using the spherically averaged data of the three-dimensional simulations in Chon et al. (2016): We set the initial surface density as

$$\Sigma(r) = \int_{-(r_{\rm out}^2 - r^2)^{1/2}}^{(r_{\rm out}^2 - r^2)^{1/2}} \tilde{\rho}\left(\sqrt{r^2 + z^2}\right)\,{\rm d}z, \tag{30}$$

and the initial angular velocity as

$$\Omega(r) = \frac{\tilde{v}_\phi(r)}{r}, \tag{31}$$

where $\tilde{\rho}$ is the spherically averaged density as a function of $(r^2 + z^2)^{1/2}$ and $\tilde{v}_\phi$ is the density-weighted spherical average of the rotational velocity, which is almost identical to the rotational velocity in the equatorial plane because the density is larger in the equatorial plane than in the polar direction. Approximately, the density and the angular velocity are constant in the core, but decrease in proportion to r^{-2} and $r^{-1/2}$ in the envelope, respectively.

The initial temperature and chemical fractions of H, H$_2$, H$^+$, and e are set to the values obtained from the one-zone calculation when the number density reaches 10^5 cm^{-3}. In our thermal and chemical models, we consider the effects of external radiation from a nearby galaxy. Following Chon et al. (2016), we set the values of the far-UV intensity J_{21} to 5000 for the *filamentary* cloud and 1000 for the *spherical* cloud (see equation 23).

3 RESULT

Here, we show our simulation results for the *filamentary* and *spherical* clouds. We present the time evolution of the discs around the central stars in Section 3.1 and the growth of central stars due to the intermittent accretion from the discs in Section 3.2. In Section 3.3, we compare our results with a run using the barotropic temperature–density relation.

3.1 Time evolution of the gravitationally unstable disc

Fig. 1 shows the time evolution of the disc in the *filamentary* cloud. In the figure, we present the surface density (top panel), the temperature (middle panel), and the chemical fraction of H$_2$ (bottom panel) at four different times, 5, 10, 20, and 30 kyr after the disc formation.

In the initial stage of gravitational collapse, the inner gas falls directly to the central sink cell because the angular momentum is lower at smaller radius in the initial condition. As time passes, the infalling gas starts rotating around the sink and forming a disc because the outer gas with high angular momentum hits the centrifugal barrier near the sink cell and cannot fall directly to the sink. The disc becomes massive and gravitationally unstable soon after its formation due to the large mass supply rate to the disc. By 5 kyr after the disc formation, the gravitational instability leads to the formation of spiral arms and dozens of clumps, as seen in the surface density panel of Fig. 1. Most of the clumps are confined to a compact central area of 5000 au in the early phase (5 and 10 kyr), but they later spread to a wider area of 10 000 au, creating a central cavity region of 5000–10 000 au (20 and 30 kyr). The clumps tend to rotate at outer radius as the angular momentum is brought in by the gas supplied from the envelope. The clumps form in the high-density parts of the spiral arms created due to the collisions of spiral arms. Most clumps end up with falling down to the centre, maintaining the high accretion rate to the sink cell, as we will see in Section 3.2.

The temperature of the envelope is quasi-isothermal with 5000–8000 K, consistent with the one-zone calculation of a gravitationally collapsing core (Fig. B1), whereas that of the disc varies by three orders of magnitude (10^2–10^5 K) and largely different from the

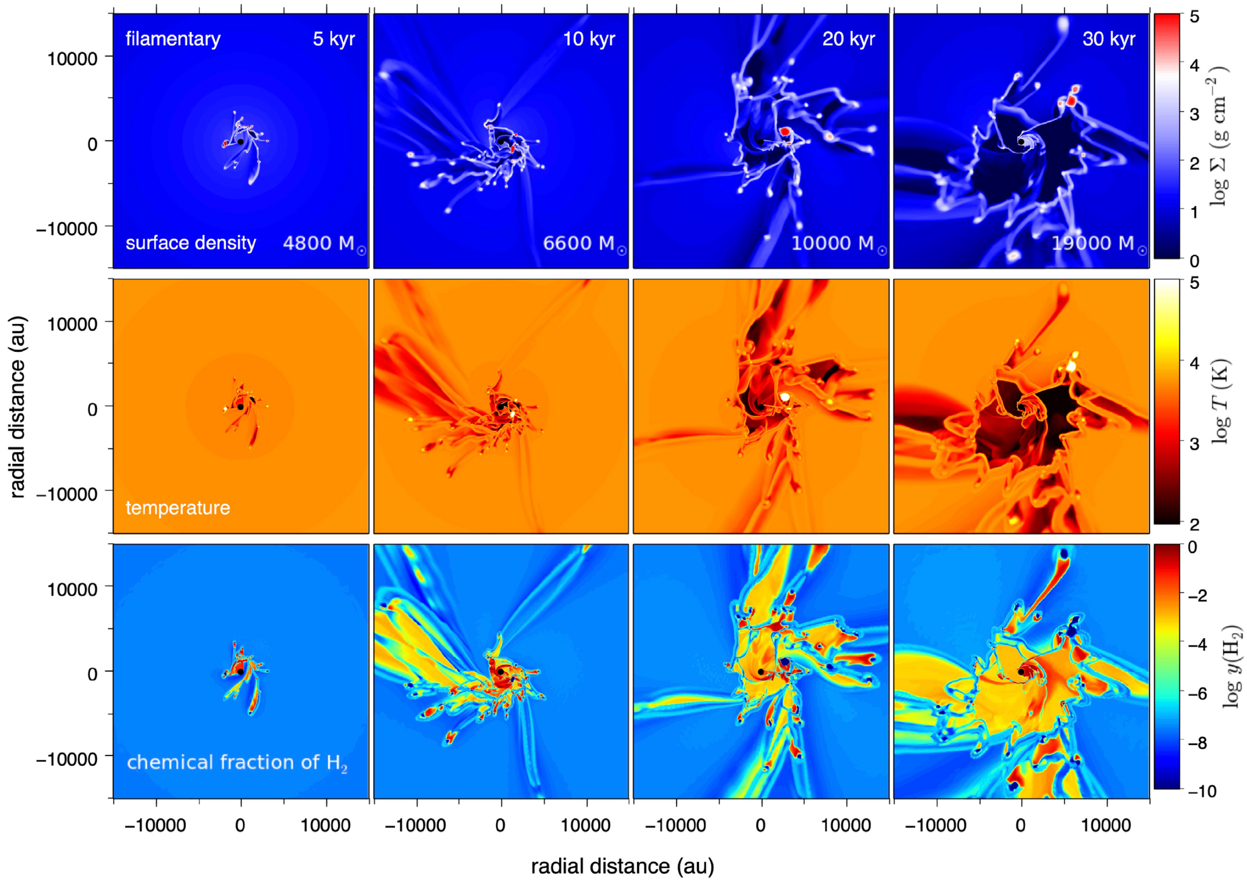

Figure 1. The time evolution of the disc in the *filamentary* cloud. Each row corresponds to the surface density (top panel), temperature (middle panel), and chemical fraction of H_2 (bottom panel) at four different times, 5, 10, 20, and 30 kyr after the disc formation. The central stellar mass at each time is shown in the bottom right-hand corner of the upper panels.

results of the one-zone calculation. The temperature is closely related to the density structures: it is high in the clumps ($>10^4$ K), low behind the spiral arms ($\sim$1000 K; the rotation is counterclockwise on this paper), and even lower in the cavity region ($\sim 10^2$ K; see the panels at 20 and 30 kyr). The chemical fraction of H_2 is inversely correlated with the temperature: $y(\mathrm{H_2})$ is $\sim 10^{-6}$ in the envelope and spiral arms where the temperature is moderate, smaller ($<10^{-10}$) in the hot clumps, and higher ($\gtrsim 10^{-3}$) in the region behind the spiral arms and the cavity region where the temperature is low.

Fig. 2 shows the time evolution of the disc in the *spherical* cloud, which is qualitatively the same as in the *filamentary* cloud. The disc is gravitationally unstable and fragmented to spiral arms and clumps, whose distributions spread spatially with time.

In both runs, some clumps are ejected from the vicinity of the central star as a result of the gravitational interactions with the central star or other clumps. An ejected clump can survive as a single star if its velocity is larger than the escape velocity,

$$u_{\mathrm{esc}} = \left(\frac{2GM_*}{R}\right)^{1/2} \simeq 23\ \mathrm{km\ s^{-1}} \left(\frac{M_*}{3\times 10^4\,M_\odot}\right)^{1/2} \left(\frac{10^5\ \mathrm{au}}{R}\right)^{1/2}, \quad (32)$$

where R is the radial distance of the ejected clump from the central star. For the *filamentary* cloud, the two clumps locating at $R = 6\times 10^4$ and 8×10^4 au at the end of the calculation have the velocities (35 and 47 km s^{-1}, respectively) exceeding the escape velocity (equation 32), and would escape from the system thereafter. For the *spherical* cloud, on the other hand, no clump is found to have high enough velocity to escape.

In the following, we give detailed analyses of the disc structures to get a deeper understanding of the disc evolution. Here, we present the analyses only for the *filamentary* cloud because those for the *spherical* cloud are similar, as expected from the similar time evolution seen in Figs 1 and 2.

In order to examine the gravitational instability of the disc, we plot in Fig. 3 the spatial distributions of Toomre's Q parameter (Toomre 1964),

$$Q_{\mathrm{T}} = \frac{c_{\mathrm{s}}\Omega}{\pi G\Sigma}, \quad (33)$$

where we have replaced the epicyclic frequency with $\Omega = v_\phi/r$ assuming quasi-Keplerian rotation. From the Toomre's criterion, the disc is gravitationally unstable in the region with $Q_{\mathrm{T}} < 1$ (purple), marginally stable in the region with $Q_{\mathrm{T}} = 1$ (white), and stable in the region with $Q_{\mathrm{T}} > 1$ (green). It is clear from the comparison with Fig. 1 that the distribution of Q_{T} is closely related to the distributions of the surface density and temperature (they are also closely related each other as mentioned above): The high-density regions (i.e. clumps) have $Q_{\mathrm{T}} < 1$, while the low-density regions has $Q_{\mathrm{T}} > 1$; the spiral arms have $Q_{\mathrm{T}} \approx 1$, which means they are in the critical state of disc fragmentation. This value of Q_{T} along the spiral arms confirms that the gravitational instability of disc in fact causes their formation. The distribution of Q_{T} is consistent with a picture of gravitationally

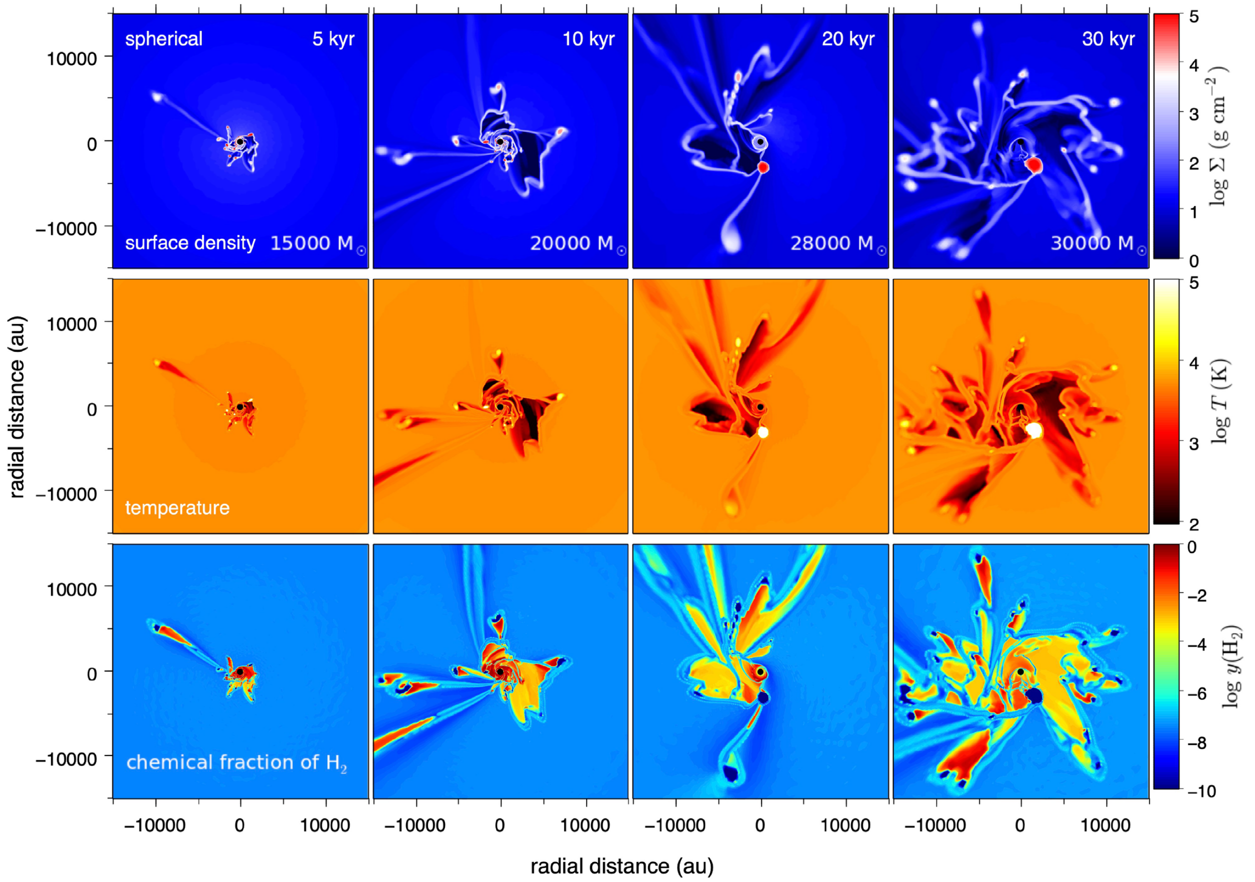

Figure 2. Same as Fig. 1, but for the *spherical* cloud.

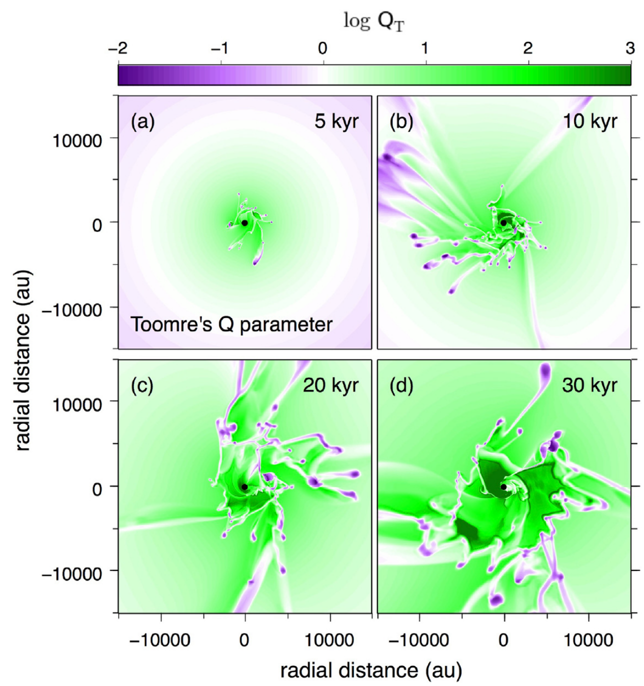

Figure 3. Spatial distributions of Toomre's Q parameter in the *filamentary* cloud. The time of each panel is the same as in Fig. 1.

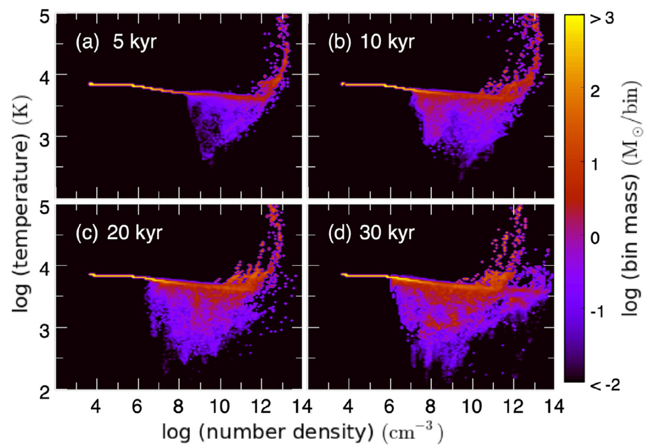

Figure 4. Gas mass distributions on the density–temperature phase diagrams for the *filamentary* cloud. The colour indicates the mass in each density–temperature bin with the widths of $\Delta \log n_\mathrm{H} = 0.1$ and $\Delta \log T = 0.025$. The time of each panel is the same as in the Fig. 1.

unstable discs in which the gravitational torque of spiral arms and clumps drives the accretion flows (e.g. Matsukoba et al. 2019).

The gravitational instability of the disc depends on the temperature of the gas since $Q_\mathrm{T} \propto c_\mathrm{s}$ from equation (33). To understand the thermal evolution of gas, we plot the mass distributions on the density–temperature phase diagrams in Fig. 4. In all four panels, a large amount of gas is distributed isothermally with the temperature

$\sim$5000–8000 K between the number density $\sim 10^3$ and 10^8 cm^{-3}. This is the envelope contracting due to the atomic hydrogen cooling. The low-temperature (< 1000 K) regions with the number density 10^7–10^{11} cm^{-3} correspond to the regions behind the spiral arms. When the spiral arms pass through and sweep out the gas, not only the density but also the temperature significantly decreases. The decrease of the temperature is roughly adiabatic ($T \propto \rho^{2/3}$) because the expansion cooling works as the main coolant. Other features evident in the figure are the high-density ($>10^{11}$ cm^{-3}) and high-temperature ($>10^4$ K) regions that correspond to the optically-thick clumps heated due to adiabatic contraction.

Next, we examine the one-dimensional structure of the disc. The radial profiles of the azimuthally averaged (panel a) surface density, (panel b) temperature, and (panel c) the enclosed mass in the *filamentary* cloud are shown in Fig. 5. Along with the profiles at 5 (red), 10 (orange), 20 (green), and 30 (blue) kyr after the disc formation, we plot the radial profiles of the one-dimensional steady accretion disc model in Matsukoba et al. (2019) with the grey filled lines, for which we set the two parameters of the model, the stellar mass, and accretion rate, to 5000–30 000 $M_\odot$ and 0.1 $M_\odot$ yr^{-1}, respectively. In this one-dimensional model, we solve the non-equilibrium chemical and thermal evolution assuming that the disc is marginally unstable with $Q_\mathrm{T} = 1$. Here, we adjust the the outer edge of the disc to 10^4 au (it was 10^3 au in Matsukoba et al. 2019), but otherwise adopt the same set-up as in Matsukoba et al. (2019).

At each time, we see a strong density peak with 10^3–10^4 g cm^{-2} at 10^3–10^4 au (Fig. 5a), which is coincided with a temperature peak with $\gtrsim 10^4$ K (Fig. 5b). The peak corresponds to the largest clump at each time, which is seen as the largest red clump in each panel of the surface density snapshots in Fig. 1. These clumps are actually the identical clump observed at a different time, which we have confirmed from the snapshots with short time intervals. The clump mass, which can be estimated from the jumps in the enclosed mass profile (Fig. 5c), is $\sim$1000 $M_\odot$ at 5 kyr and grows to $\sim$10 000 $M_\odot$ at 30 kyr, as a result of mergers with other clumps and accretion of surrounding gas. While the clump grows in mass, it also acquires the angular momentum through the growth process, and thus its separation from the centre gradually expands, as indicated by the position of the peak moving outward with time in Fig. 5. Similar orbital evolution was reported in the simulations of Pop III star formation (Chon & Hosokawa 2019; Sugimura et al. 2020).

Now, let us briefly compare the simulation results with the one-dimensional steady accretion disc model. In Fig. 5 (a and b), the radial profiles of surface density and temperature are roughly consistent with the one-dimensional model outside the peaks, but largely different inside the peaks, where the surface density is two to three orders of magnitude smaller than that of the one-dimensional model and the temperature drops from $\sim$3000 to 1000 K due to the expansion cooling. This lower surface density implies that the gap opening is induced by the gravitational interaction of the central star, the largest clump, and infalling gas. The one-dimensional model fails to reproduce the simulation results because such effect is not taken into account.

Before closing this section, it is worth noticing that massive clumps are formed in both the *filamentary* and *spherical* clouds (see the upper right-hand panels in Figs 1 and 2). We show the mass evolution of the central star and the largest clump in Fig. 6. Here the mass of the largest clump is calculated by summing the mass in the grids with the surface density above 10^4 g cm^{-2} around the maximum density in the clump, which is sampled at every 5 kyr starting from 5 kyr after the disc formation. The largest clump has grown to 17 000 (*filamentary*) and 21 000 (*spherical*) $M_\odot$ and locates at $\sim 10^4$ (*filamentary*) and 3×10^3 (*spherical*) au away from the central star at the end of the calculations (at $\sim$50 and 30 kyr after the disc formation, respectively), when the central stellar masses reach 30 000 $M_\odot$. The largest clump in each run potentially makes a binary stellar system with the central star eventually (see also Section 4). Although longer time-scale calculation is required to draw definite conclusion, previous simulations in a similar context have observed the formation of binary SMSs (Chon et al. 2018; Latif, Khochfar & Whalen 2020).

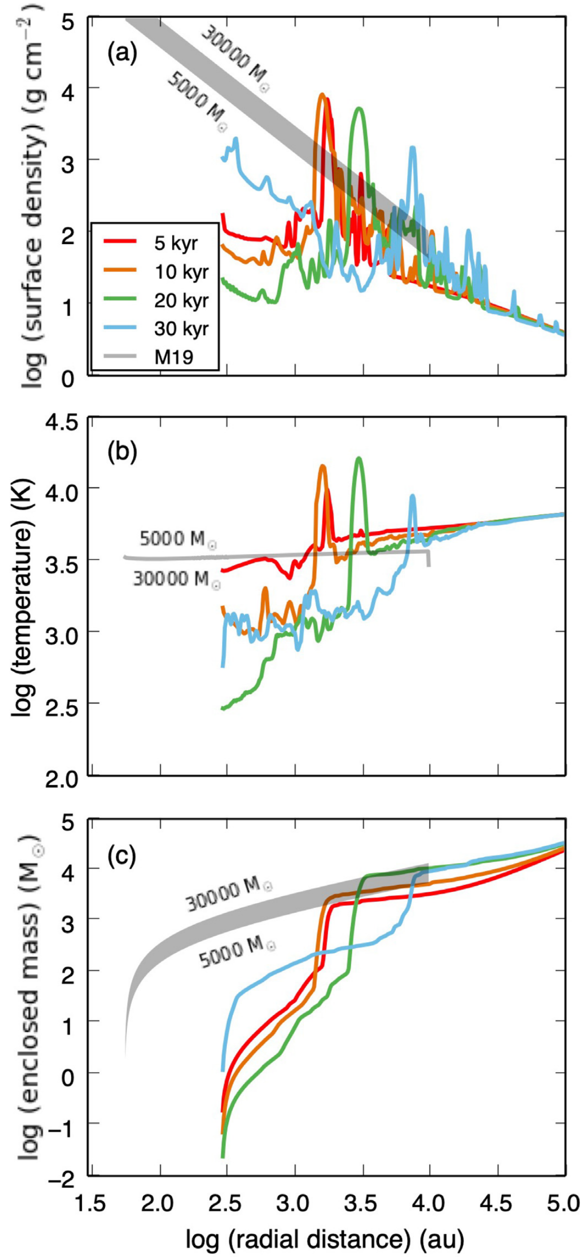

Figure 5. Radial profiles of the azimuthally averaged (panel a) surface density, (panel b) temperature, and (panel c) the enclosed mass in the *filamentary* cloud. The grey filled lines show the radial profiles of the one-dimensional steady accretion disc model (Matsukoba et al. 2019) for the stellar mass between 5000 and 30 000 $M_\odot$. The colours indicate the times after the disc formation, 5 (red), 10 (orange), 20 (green), and 30 kyr (blue), when the stellar masses are 4800, 6600, 10 000, and 19 000 $M_\odot$, respectively.

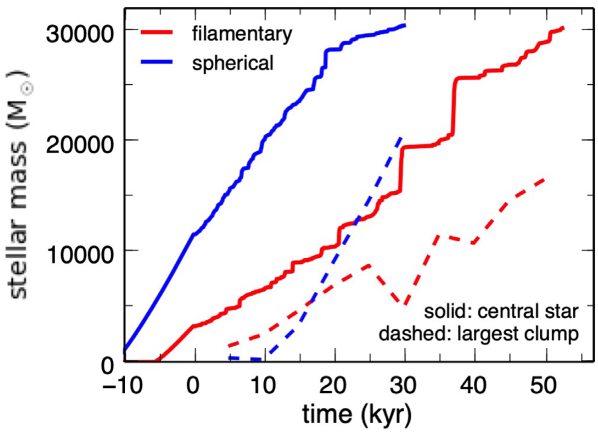

Figure 6. Time evolution of the star and the largest clump masses. The colours correspond to *filamentary* cloud (red) and *spherical* cloud (blue). The solid and dashed lines represent the central stellar mass and the largest clump mass, respectively.

3.2 Stellar evolution under intermittent accretion

In Fig. 6, the stellar masses reach the final mass of 30 000 $M_\odot$ in both cases, but the growth time is shorter in the *spherical* cloud than in the *filamentary* cloud (∼30 and ∼50 kyr, respectively). The central star accretes the gas more rapidly in the *spherical* cloud because the *spherical* cloud has the smaller initial angular momentum than the *filamentary* cloud.

Fig. 7 shows the accretion rates in the two cases. We plot the time-averaged rates with bins of 1000 yr (blue) along with the raw rates (red). The raw accretion rates violently fluctuate by nine orders of magnitude in both cases, while the averaged rates fluctuate much more gently with some occasional strong bursts. We attribute the strong fluctuations of the averaged rates to the interaction with the massive clumps that have the masses comparable to the central stars, as explained in Section 3.1. In contrast, the fluctuation of the averaged rate is especially small in the early time ($\lesssim$15 kyr) in the *spherical* cloud, partly because clumps as massive as the central star has yet to form for this period. The massive clumps exert gravitational torque on the gas in the discs, causing accretion bursts that are followed by short quiescent periods. Besides, they sometimes approach the central star so closely as to be tidally disrupted and some of their material is transferred to the central star, as we observe in the snapshots with short time intervals. Such events cause the particularly large accretion bursts at ∼30 and 38 kyr in the *filamentary* cloud, which increase the stellar mass by ∼5000 $M_\odot$ (see also Fig. 6).

As described in the introduction, the radiative feedback by the ionizing radiation from the protostars may quench the accretion if the accretion rate drops below the critical value of $4 \times 10^{-2}\ M_\odot\ \mathrm{yr}^{-1}$ (black dashed line in Fig. 7; Hosokawa et al. 2012, 2013) and cannot keep the stellar surfaces inflated. According to Sakurai et al. (2015), if a quiescent period Δt_q, for which the accretion rate is below the critical value, is longer than the KH time-scale at the stellar surface $t_\mathrm{KH,\,surf}$ (equation 1), the radiative feedback quenches the accretion because the stellar surface shrinks significantly and the associated rise of the effective temperature leads to the emission of strong ionizing radiation. Conversely, if $\Delta t_\mathrm{q} < t_\mathrm{KH,\,surf}$, the radiative feedback is ineffective because the contracting stellar surface turns to inflating due to the revival of the accretion rate before the strong ionizing radiation is emitted.

Below we estimate the effect of radiative feedback in our simulated cases, using the above condition. In the *filamentary* cloud, the longest quiescent period $\Delta t_\mathrm{q} \sim 2000$ yr at $t = 38$ kyr is shorter than the KH time-scale $t_\mathrm{KH,\,surf} \sim 7000$ yr for the stellar mass of ∼25 000 $M_\odot$ at this time (equation 1). Similarly, in the *spherical* cloud, the longest quiescent period $\Delta t_\mathrm{q} \sim 800$ yr at $t = 20$ kyr is shorter than the KH time-scale $t_\mathrm{KH,\,surf} \sim 7500$ yr for the stellar mass of ∼28 000 $M_\odot$ at this time. There are other quiescent periods with $\Delta t_\mathrm{q} \sim 700$ yr at $t =$ 33, 44, and 46 kyr in the *filamentary* cloud, but they are all about one order of magnitude shorter than the KH time-scales. Therefore, in our simulated cases, the quiescent periods never exceed the KH time-scales, and thus we conclude that the radiative feedback by ionizing radiation, although not explicitly considered in our simulations, does not affect the accretion flows.

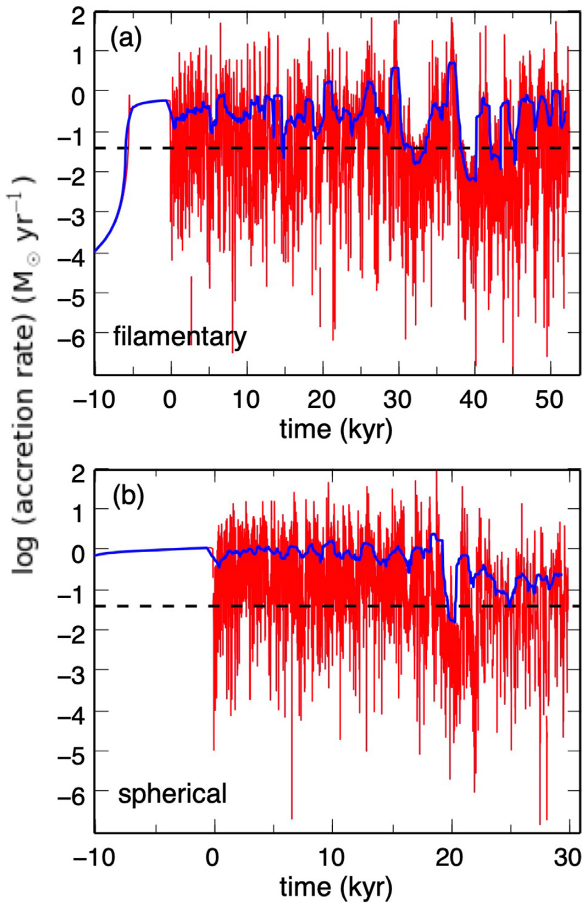

Figure 7. Accretion histories on to the central star with different initial conditions: (panel a) *filamentary* cloud and (panel b) *spherical* cloud. The red line represents the raw accretion rate, and the blue line denotes the time-averaged rate with bin of 1000 yr. The black dashed line indicates the critical rate ($4 \times 10^{-2}\ M_\odot\ \mathrm{yr}^{-1}$), below which the star begins to emit ionizing photons due to stellar contraction if the accretion rate is constant.

In the both runs studied, the largest clump is as massive as the central star. The gas surrounding that clump, however, is not affected so much by the radiative feedback from the star formed there because the accretion rate is higher than the critical value: 0.1 for the *filamentary* and 0.2 $M_\odot\ \mathrm{yr}^{-1}$ for the *spherical* cloud from Fig. 6.

3.3 Comparison with the calculation using a barotropic relation

In this section, we compare our main run described above with an additional run using a barotropic temperature-density relation, as in

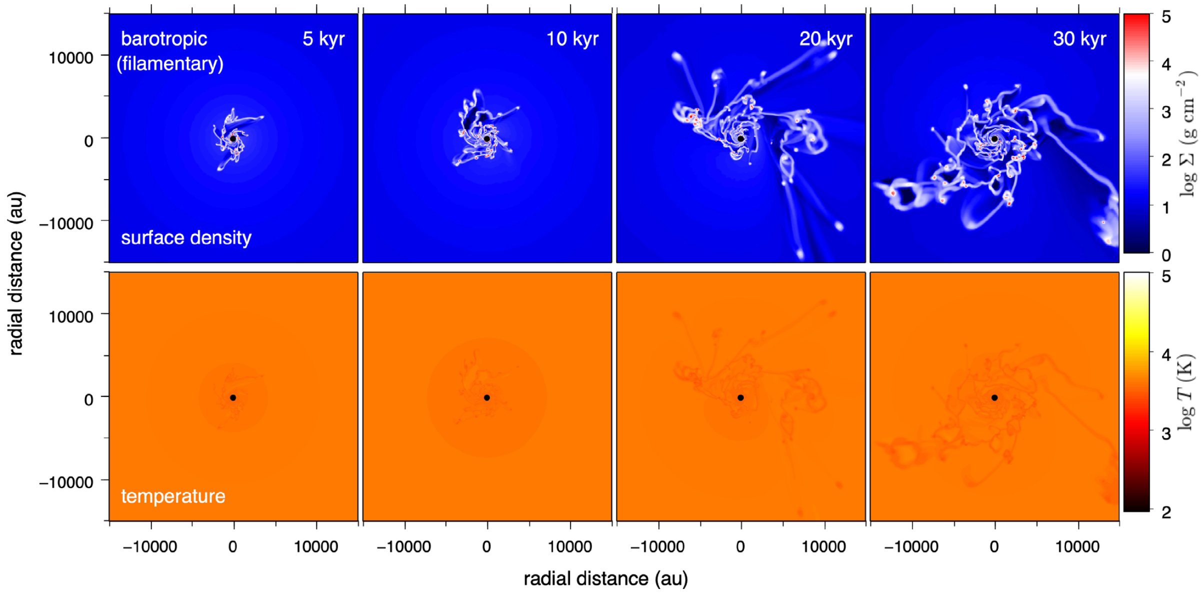

Figure 8. Same as Fig. 1, but for the run with a barotropic relation starting from the initial condition of the *filamentary* cloud. The spatial distributions of surface density (upper panels) and temperature (lower panels) are shown.

the previous study (Sakurai et al. 2016), focusing on the case of the *filamentary* cloud. Fig. 8 shows the spatial distributions of the surface density and temperature in the run starting from the same initial condition of the *filamentary* cloud but using the barotropic relation instead of solving the energy equation.

In the upper panels of Fig. 8, the circumstellar disc is fragmented into a large number of spiral arms and clumps from an early stage and their number further increases with time. While the runs with our thermal model and the barotropic relation commonly show the fragmentation of the discs into spiral arms and clumps, we find two major differences regarding the properties of the clumps: (1) The number of clumps in the run with the barotropic relation is larger than in the run with our thermal model, and (2) the massive clumps found in the run with our thermal model is not found in the run with the barotropic relation. The dependence of the characteristics of clumps on the adopted thermal model was also argued in the case of Pop III star formation (Clark et al. 2011).

We attribute these differences mainly to the lack of resolution in the run with the barotropic relation. The local Jeans length must be resolved by at least four grids in order to avoid artificial fragmentation (Truelove et al. 1997). In the barotropic run, however, we find that this condition is not satisfied near clumps. With the barotropic relation, the local Jeans length at (10^{16} cm^{-3}, 7000 K), where the gas becomes adiabatic, is

$$\lambda_J = 1.3 \text{ au} \left(\frac{n_H}{10^{16}\ \text{cm}^{-3}}\right)^{-1/2} \left(\frac{T}{7000\ \text{K}}\right)^{1/2}. \quad (34)$$

In late stages of the run, clumps are distributed within around 5000 au from the central star, where the grid size is 80 au. This means the local Jeans length around the clump location is far below the resolution: The required number of grids for the Truelove et al. (1997) criterion is more than 250 times that in our calculations. Consequently, artificial fragmentation of the clumps sometimes takes place.

The temperature distributions in the run with the barotropic relation, as shown in the lower panels of Fig. 8, is largely different from those in the run with our thermal model (Fig. 1). In the run with our thermal model, the temperature varies by three orders of magnitude (100–10^5 K), mainly due to the compressional/shock heating and the expansion cooling associated with the dynamics of spiral arms and clumps. In the run with the barotropic relation, however, the gas remains almost isothermal with ∼5000–8000 K because the barotropic relation is calculated without taking into account the thermal processes associated with the gas dynamics in the disc.

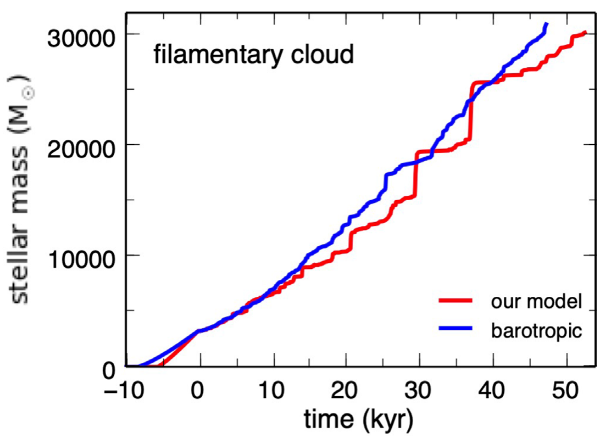

Figure 9. The dependence of time evolution of stellar mass on the treatment of thermal evolution. We show the results from the runs starting from the initial condition of the *filamentary* cloud with our thermal model (red) and the barotropic relation (blue).

In Fig. 9, we compare the time evolution of the central stellar masses in the runs with our thermal model (red) and the barotropic relation (blue). We also provide the time evolution of the accretion rate in the run with the barotropic relation in Fig. 10 (see Fig. 7 a for the run with our thermal model). While the stellar masses reach 30 000 $M_\odot$ around the same time (∼50 kyr) in both runs, the mass growth is smoother and the time-averaged accretion rate never falls below the critical rate in the run with the barotropic relation because smaller but more numerous clumps are formed and continuously accrete on to the central star. This implies that runs with the barotropic

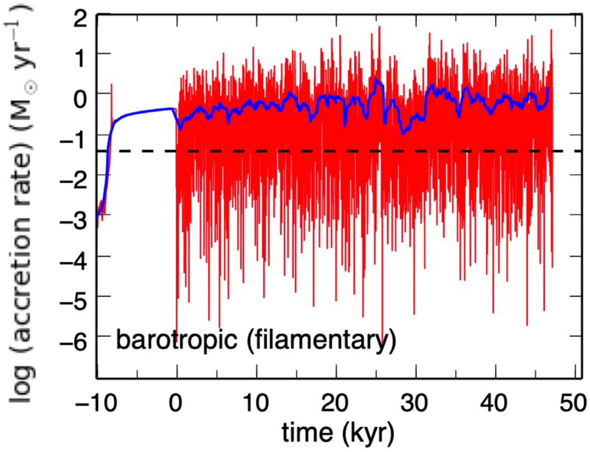

Figure 10. Same as Fig. 7, but for the run starting from the initial condition of the *filamentary* cloud with the barotropic relation.

relation underestimate the length of quiescent periods. Although the quiescent periods are shorter than the KH time-scales in our examined cases, as explained in Section 3.2, the radiative feedback still potentially prevents the accretion in some cases. In such cases, the use of the barotropic relation may lead to a wrong conclusion on the role of the radiative feedback. Therefore, realistic treatment of the thermal evolution is crucial to understand the SMS formation.

4 SUMMARY AND DISCUSSION

SMSs are prominent candidate objects for the origin of SMBHs observed in the early Universe. In this paper, we have investigated the time evolution of the discs around growing SMSs by performing vertically integrated two-dimensional hydrodynamic simulations starting from two cosmological initial conditions named *filamentary* and *spherical* clouds (Chon et al. 2016). We have put a particular focus on the time variation of the accretion rate, because it was known that the ionizing radiation from a protostar can terminates the gas accretion, and hence the stellar growth, if the quiescent period of the intermittent accretion is longer than the KH time-scale at the stellar surface (Sakurai et al. 2015).

In both the *filamentary* and *spherical* clouds, gravitationally unstable circumstellar discs that are fragmented into spiral arms and clumps provide the central stars with gas in an intermittent way. The longest quiescent periods are 2000 (*filamentary*) and 800 (*spherical*) yr and shorter than the KH time-scales of 7000 (*filamentary*) and 7500 yr (*spherical*), respectively, suggesting that protostars can continue to grow until they become SMSs without affected by the ionizing radiation. By the time the central star have grown to 30 000 $M_\odot$, the largest clump around it reaches 17 000 (*filamentary*) and 21 000 $M_\odot$ (*spherical*), respectively. The system may evolve to a binary SMS and eventually become a binary BH.

Furthermore, we have compared our results with an additional run adopting the same initial condition but using the barotropic temperature–density relation, as in the previous work (Sakurai et al. 2016). In this run, the quiescent periods are shorter because smaller but more numerous clumps are formed and continuously accrete on to the central star. Thus, we have found that without solving the thermal and chemical evolution, one tends to underestimate the length of quiescent periods and may come to a wrong conclusion on the role of the radiative feedback. Moreover, although we have observed the formation of binary SMSs in both of the runs with our thermal model, only small clumps form in the run with the barotropic relation. From these reasons, we conclude that the simulations using the barotropic relation cannot describe the actual formation processes of SMSs.

Chon et al. (2018) studied the SMS formation using three-dimensional simulations with the same initial conditions as ours. They observed the formation of only 25 (*filamentary*) and 13 (*spherical*) clumps in each cloud, although we have observed the formation of more than hundred clumps in each cloud. Below, we provide three effects that probably play some roles in causing this difference. First, our simulations have higher effective resolution than their smoothed-particle hydrodynamic simulations. In Chon et al. (2018), they assumed that the gas becomes adiabatic at the density higher than 10^{13} cm^{-3} to save the computational costs, effectively setting the minimum resolution of about 40 au. As our minimum grid size is 5 au near the inner boundary at 300 au, we can follow the formation of smaller clumps in the inner region. Secondly, gravitational instability was suppressed in Chon et al. (2018) by the higher disc temperature than in our simulations. Since they did not consider the H$^-$ free–bound emission, which is the primary cooling process in the disc, the disc temperature was higher than ours. Finally, dense parts of spiral arms that are supposed to fragment into clumps are more easily formed in our simulations because in two-dimensional simulations, the vertically extended structures are confined to the disc plane and the density increases associated with the collision of spiral arms may be overestimated. Recently, Latif et al. (2020) studied the long-term ($\sim$1 Myr) evolution of forming SMSs using three-dimensional adaptive mesh refinement simulations. They also found the formation of multiple clumps, but their number is only ten or less in each run partly because their resolution was much worse than ours with the minimum grid size of 2000 au. Regan et al. (2020) also performed the three-dimensional simulations with similar resolution in Latif et al. (2020) and found more than 20 massive stars with $>$1000 $M_\odot$. Unlike in our runs, however, those stars are formed via the fragmentation of the cloud core rather than via the disc fragmentation.

In each run, a clump reaches a comparable mass with the central star. Its orbital distance from the central star is 2000 au in the early phase ($\sim$5 kyr) and gradually increases with time, finally reaching 9000 (*filamentary*) and 4000 au (*spherical*), respectively. We expect the separation will increase even after that owing to the acquisition of angular momentum by the gas accretion, as suggested in recent simulations of binary accretion (Duffell et al. 2020; Muñoz et al. 2020). In fact, long-term simulations in Latif et al. (2020) demonstrated the formation of binary SMSs with a wide separation ($\sim$pc). The massive clumps in our runs may also make binary SMSs with their central stars. If such a binary system survives without merger until the end of the SMS lifetime, the outcome will be a binary BH system with $\gtrsim$ 10 000 $M_\odot$ (Umeda et al. 2016). The merger of such binary BHs is particularly important because the gravitational waves from the merger event will be detectable by next-generation gravitational wave detectors, e.g. Deci-hertz Interferometer Gravitational wave Observatory (DECIGO: Kawamura et al. 2011) and Laser Interferometer Space Antenna (LISA: Amaro-Seoane et al. 2012). As the accretion on to each star and the associated orbital evolution of the binaries still continue at the end of our simulations, it is necessary to carry out long-time simulations to address the properties of the binary BHs.

Our numerical results depend somewhat on the resolution because we cut off the cooling at high-density regions using equations (28) and (29). In order to examine the effect of the resolution, we have carried out the additional runs with 256 $\times$ 256 and 768 $\times$ 768 grids (while with 512 × 512 grids in our runs so far) until 10 kyr after the disc formation. We found that the number of small fragments increases toward higher resolution, while a binary star system emerges at the centre in the both runs. The quiescent period is at most ∼100 yr in both runs and always shorter than the KH time-scale. The length of quiescent period does not change with the resolution because the number of small fragments does not change so much the quiescent period as we mentioned in Section 3.3.

Among the effects not considered in this work, the increase of stellar spin due to the accumulation of the angular momentum of accreted gas may play a role in ceasing the stellar growth. To maintain the accretion, the sum of the radiative and centrifugal forces must be smaller than the gravity on the stellar surface, which is known as the $\Omega\Gamma$ limit (see, e.g. Maeder & Meynet 2000, Lee & Yoon 2016, Takahashi & Omukai 2017; Haemmerlé et al. 2018). We need to investigate the angular momentum transport at the interface of discs and stellar surfaces, to follow the stellar spin evolution and understand the role of the $\Omega\Gamma$ limit in the SMS formation.

Although our simulations have followed the formation process of SMSs for ∼30–50 kyr, longer time (∼Myr) simulations are needed to decide the fate of growing SMSs. Moreover, three-dimensional simulations are needed to consider vertical gas dynamics missed in our simulations. In future studies, we will come back to high-resolution long-term three-dimensional simulations, to reveal the true nature of SMS formation.

ACKNOWLEDGEMENTS

RM acknowledges financial support from the Graduate Program on Physics for Universe of Tohoku University. EIV acknowledges support from the Austrian Science Fund (FWF) under research grant P31635-N27. KS appreciates the support by the Fellowship of the Japan Society for the Promotion of Science for Research Abroad. This work is financially supported by the Grants-in-Aid for Basic Research by the Ministry of Education, Science and Culture of Japan (SC:19J00324, TH:19H01934, KO:17H02869, 17H01102, 17H06360). The numerical simulations were carried out on XC50 at the Center for Computational Astrophysics (CfCA) of National Astronomical Observatory of Japan.

DATA AVAILABILITY

The data underlying this paper will be shared on reasonable request to the corresponding author.

REFERENCES

Amaro-Seoane P. et al., 2012, Class. Quantum Gravity, 29, 124016
Bañados E. et al., 2018, Nature, 553, 473
Becerra F., Greif T. H., Springel V., Hernquist L. E., 2015, MNRAS, 446, 2380
Becerra F., Marinacci F., Inayoshi K., Bromm V., Hernquist L. E., 2018, ApJ, 857, 138
Bromm V., Loeb A., 2003, ApJ, 596, 34
Cen R., 1992, ApJS, 78, 341
Chon S., Hirano S., Hosokawa T., Yoshida N., 2016, ApJ, 832, 134
Chon S., Hosokawa T., 2019, MNRAS, 488, 2658
Chon S., Hosokawa T., Yoshida N., 2018, MNRAS, 475, 4104
Clark P. C., Glover S. C. O., Klessen R. S., Bromm V., 2011, ApJ, 727, 110
Croft H., Dickinson A. S., Gadea F. X., 1999, MNRAS, 304, 327
Dove J. E., Rusk A. C. M., Cribb P. H., Martin P. G., 1987, ApJ, 318, 379
Draine B. T., Bertoldi F., 1996, ApJ, 468, 269
Duffell P. C., D'Orazio D., Derdzinski A., Haiman Z., MacFadyen A., Rosen A. L., Zrake J., 2020, ApJ, 901, 25
Ferland G. J., Peterson B. M., Horne K., Welsh W. F., Nahar S. N., 1992, ApJ, 387, 95
Fukushima H., Omukai K., Hosokawa T., 2018, MNRAS, 473, 4754
Gallerani S., Fan X., Maiolino R., Pacucci F., 2017, Publ. Astron. Soc. Aust., 34, e022
Glover S., 2008, in O'Shea B. W., Heger A., eds, AIP Conf. Ser. Vol. 90, First Stars III. Am. Inst. Phys., New York, p. 25
Glover S. C. O., 2015, MNRAS, 453, 2901
Haemmerlé L., Woods T. E., Klessen R. S., Heger A., Whalen D. J., 2018, ApJ, 853, L3
Haemmerlé L., Woods T. E., Klessen R. S., Heger A., Whalen D. J., 2018a, MNRAS, 474, 2757
Haiman Z., 2013, in Wiklind T., Mobasher B., Bromm V., eds, Astrophysics and Space Science Library, Vol. 396, The First Galaxies. Springer-Verlag, Berlin and Heidelberg, p. 293
Hosokawa T., Hirano S., Kuiper R., Yorke H. W., Omukai K., Yoshida N., 2016, ApJ, 824, 119
Hosokawa T., Omukai K., Yorke H. W., 2012, ApJ, 756, 93
Hosokawa T., Yorke H. W., Inayoshi K., Omukai K., Yoshida N., 2013, ApJ, 778, 178
Inayoshi K., Haiman Z., 2014, MNRAS, 445, 1549
Inayoshi K., Haiman Z., Ostriker J. P., 2016, MNRAS, 459, 3738
Inayoshi K., Omukai K., Tasker E., 2014, MNRAS, 445, L109
Inayoshi K., Visbal E., Haiman Z., 2020, ARA&A, 58, 27
Janev R. K., Langer W. D., Evans K., 1987, Elementary Processes in Hydrogen-Helium Plasmas – Cross Sections and Reaction Rate Coefficients. Springer-Verlag, Berlin and Heidelberg
John T. L., 1988, A&A, 193, 189
Kawamura S. et al., 2011, Class. Quantum Gravity, 28, 094011
Kreckel H., Bruhns H., Čížek M., Glover S. C. O., Miller K. A., Urbain X., Savin D. W., 2010, Science, 329, 69
Latif M. A., Khochfar S., Whalen D., 2020, ApJ, 892, L4
Latif M. A., Schleicher D. R. G., 2015, A&A, 578, A118
Latif M. A., Schleicher D. R. G., Schmidt W., Niemeyer J. C., 2013, MNRAS, 436, 2989
Lee H., Yoon S.-C., 2016, ApJ, 820, 135
Lenzuni P., Chernoff D. F., Salpeter E. E., 1991, ApJS, 76, 759
Madau P., Rees M. J., 2001, ApJ, 551, L27
Maeder A., Meynet G., 2000, A&A, 361, 159
Matsukoba R., Takahashi S. Z., Sugimura K., Omukai K., 2019, MNRAS, 484, 2605
Matsuoka Y. et al., 2018, ApJS, 237, 5
Mayer M., Duschl W. J., 2005, MNRAS, 358, 614
Milosavljević M., Couch S. M., Bromm V., 2009, ApJ, 696, L146
Muñoz D. J., Lai D., Kratter K., Mirand a R., 2020, ApJ, 889, 114
Omukai K., 2001, ApJ, 546, 635
Omukai K., Palla F., 2003, ApJ, 589, 677
Onoue M. et al., 2019, ApJ, 880, 77
Palla F., Salpeter E. E., Stahler S. W., 1983, ApJ, 271, 632
Park K., Ricotti M., 2011, ApJ, 739, 2
Regan J. A., Johansson P. H., Wise J. H., 2014, ApJ, 795, 137
Regan J. A., Wise J. H., Woods T. E., Downes T. P., O'Shea B. W., Norman M. L., 2020, preprint (arXiv:2008.08090)
Sakurai Y., Hosokawa T., Yoshida N., Yorke H. W., 2015, MNRAS, 452, 755
Sakurai Y., Vorobyov E. I., Hosokawa T., Yoshida N., Omukai K., Yorke H. W., 2016, MNRAS, 459, 1137
Shakura N. I., Sunyaev R. A., 1973, A&A, 24, 337
Shang C., Bryan G. L., Haiman Z., 2010, MNRAS, 402, 1249
Sugimura K., Hosokawa T., Yajima H., Inayoshi K., Omukai K., 2018, MNRAS, 478, 3961
Sugimura K., Hosokawa T., Yajima H., Omukai K., 2017, MNRAS, 469, 62
Sugimura K., Matsumoto T., Hosokawa T., Hirano S., Omukai K., 2020, ApJ, 892, L14
Sugimura K., Omukai K., Inoue A. K., 2014, MNRAS, 445, 544

Takahashi S. Z., Omukai K., 2017, MNRAS, 472, 532
Toomre A., 1964, ApJ, 139, 1217
Trevisan C. S., Tennyson J., 2002, Plasma Phys. Control. Fusion, 44, 1263
Truelove J. K., Klein R. I., McKee C. F., Holliman John H. I., Howell L. H., Greenough J. A., 1997, ApJ, 489, L179
Umeda H., Hosokawa T., Omukai K., Yoshida N., 2016, ApJ, 830, L34
Venemans B. P. et al., 2013, ApJ, 779, 24
Volonteri M., 2012, Science, 337, 544
Vorobyov E. I., Basu S., 2009, MNRAS, 393, 822
Vorobyov E. I., Basu S., 2010, ApJ, 719, 1896
Vorobyov E. I., Matsukoba R., Omukai K., Guedel M., 2020, A&A, 638, 19
Wishart A. W., 1979, MNRAS, 187, 59P

APPENDIX A: CHEMICAL REACTIONS

We follow the compositional evolution of five species, H, H_2, H^+, H^-, and e, by solving the non-equilibrium kinetic equations. The 22 reactions included in our chemical network are summarized with their rate coefficients in Table A1. In each row where two reaction numbers are given, the first and second numbers correspond to the forward and reverse reactions, respectively. To obtain the rate coefficients for the reverse reactions, we use the method described in appendix C of Matsukoba et al. (2019).

APPENDIX B: BAROTROPIC RELATION

In Section 3.3, we describe the results from the simulation with the barotropic temperature–density relation shown in Fig. B1, for comparison with the previous study (Sakurai et al. 2016). To obtain this barotropic relation, we have carried out an one-zone calculation of the chemical and thermal evolution of a gravitationally collapsing core (Omukai 2001), using our thermal and chemical models. Using the relation between the number density and temperature in Fig. B1, with equations (5) and (7), we obtain P as a function of Σ.

Table A1. Chemical reactions.

Number	Reaction	Rate coefficient of forward reaction ($\mathrm{cm^3\ s^{-1}}$)	Reference
1, 2	$\mathrm{H + e \rightleftharpoons H^+ + 2e}$	$k_1 = \exp[-3.271\,396\,786 \times 10^1$ $+1.353\,655\,60 \times 10^1 \ln T_e - 5.739\,328\,75 \times 10^0 (\ln T_e)^2$ $+1.563\,154\,98 \times 10^0 (\ln T_e)^3 - 2.877\,056\,00 \times 10^{-1} (\ln T_e)^4$ $+3.482\,559\,77 \times 10^{-2} (\ln T_e)^5 - 2.631\,976\,17 \times 10^{-3} (\ln T_e)^6$ $+1.119\,543\,95 \times 10^{-4} (\ln T_e)^7 - 2.039\,149\,85 \times 10^{-6} (\ln T_e)^8]$	Janev, Langer & Evans (1987)
3, 4	$\mathrm{H^- + H \rightleftharpoons H_2 + e}$	$k_3 = 1.3500 \times 10^{-9}(T^{9.8493\times10^{-2}} + 3.2852 \times 10^{-1} T^{5.5610\times10^{-1}}$ $+2.7710 \times 10^{-7} T^{2.1826})/(1.0 + 6.1910 \times 10^{-3} T^{1.0461}$ $+8.9712 \times 10^{-11} T^{3.0424} + 3.2576 \times 10^{-14} T^{3.7741})$	Kreckel et al. (2010)
5. 6	$\mathrm{H_2 + e \rightleftharpoons 2H + e}$	$k_5 = k_{5,\mathrm{H}}^{1-a} k_{5,\mathrm{L}}^{a}$ $k_{5,\mathrm{H}} = 1.91 \times 10^{-9} T^{0.136} \exp\left(-53\,407.1/T\right)$ $k_{5,\mathrm{L}} = 4.49 \times 10^{-9} T^{0.11} \exp\left(-101\,858/T\right)$ $a = (1 + n_\mathrm{H}/n_\mathrm{crit})^{-1}$ $n_\mathrm{crit} = [y(\mathrm{H})/n_\mathrm{crit}(\mathrm{H}) + 2y(\mathrm{H_2})/n_\mathrm{crit}(\mathrm{H_2}) + y(\mathrm{He})/n_\mathrm{crit}(\mathrm{He})]^{-1}$ $\log(n_\mathrm{crit}(\mathrm{H})) = 3 - 0.416 \log(T/10^4) - 0.372[\log(T/10^4)]^2$ $\log(n_\mathrm{crit}(\mathrm{H_2})) = 4.845 - 1.3 \log(T/10^4) + 1.62[\log(T/10^4)]^2$ $\log(n_\mathrm{crit}(\mathrm{He})) = 5.0792[1 - 1.23 \times 10^{-5}(T - 2000)]$	 Trevisan & Tennyson (2002)
7. 8	$\mathrm{3H \rightleftharpoons H_2 + H}$	$k_7 = 7.7 \times 10^{-31} T^{-0.464}$	Glover (2008)
9, 10	$\mathrm{2H + H_2 \rightleftharpoons 2H_2}$	$k_9 = k_7/8$	Palla, Salpeter & Stahler (1983)
11, 12	$\mathrm{H^- + H^+ \rightleftharpoons 2H}$	$k_{11} = 2.4 \times 10^{-6} T^{-0.5}\left(1.0 + T/20\,000\right)$	Croft, Dickinson & Gadea (1999)
13, 14	$\mathrm{H^+ + e \rightleftharpoons H} + \gamma$	$k_{13} = 2.753 \times 10^{-14}\left(315\,614/T\right)^{1.5}\left[1.0 + \left(115\,188/T\right)^{0.407}\right]^{-2.242}$	Ferland et al. (1992)
15, 16	$\mathrm{H + e \rightleftharpoons H^-} + \gamma$	$k_{15} = \mathrm{dex}[-17.845 + 0.762 \log T + 0.1523(\log T)^2$ $-0.032\,74(\log T)^3] \quad (T < 6000\ \mathrm{K})$ $= \mathrm{dex}[-16.4199 + 0.1998(\log T)^2 - 5.447 \times 10^{-3}(\log T)^4$ $+4.0415 \times 10^{-5}(\log T)^6] \quad (T > 6000\ \mathrm{K})$	Wishart (1979)
17, 18	$\mathrm{H_2 + He \rightleftharpoons 2H + He}$	$k_{17} = k_{17,\mathrm{H}}^{1-a} k_{17,\mathrm{L}}^{a}$ $k_{17,\mathrm{H}} = \mathrm{dex}[-1.75 \log T - 2.729 - 23\,474/T]$ $k_{17,\mathrm{L}} = \mathrm{dex}[3.801 \log T - 27.029 - 29\,487/T]$	 Dove et al. (1987)
19, 20	$\mathrm{2H \rightleftharpoons H^+ + e + H}$	$k_{19} = 1.2 \times 10^{-17} T^{1.2} \exp\left(-\frac{157\,800}{T}\right)$	Lenzuni, Chernoff & Salpeter (1991)
21	$\mathrm{H_2} + \gamma_\mathrm{ex} \rightarrow \mathrm{H_2^*} \rightarrow \mathrm{2H}$	$k_{21} = 1.4 \times 10^9 J_\mathrm{ex}(h\nu = 12.4\ \mathrm{eV}) f_\mathrm{sh}$ $f_\mathrm{sh} = \min\left[1, \left(\frac{N_\mathrm{H_2}}{10^{14}\ \mathrm{cm^{-2}}}\right)^{-3/4}\right]$	Draine & Bertoldi (1996)
22	$\mathrm{H^-} + \gamma_\mathrm{ex} \rightarrow \mathrm{H + e}$	$k_{22} = [J_\mathrm{ex}(\nu)/B_\nu(T_\mathrm{ex})] k_{15}(T_\mathrm{ex})/K(T_\mathrm{ex})$ $K(T_\mathrm{ex}) = \left[\frac{n(\mathrm{H^-})}{n(\mathrm{H})n(\mathrm{e})}\right]^*$	

Notes. The temperature T_e is in eV. The value of $N_{\mathrm{H_2}}$ is the column density of molecular hydrogen.

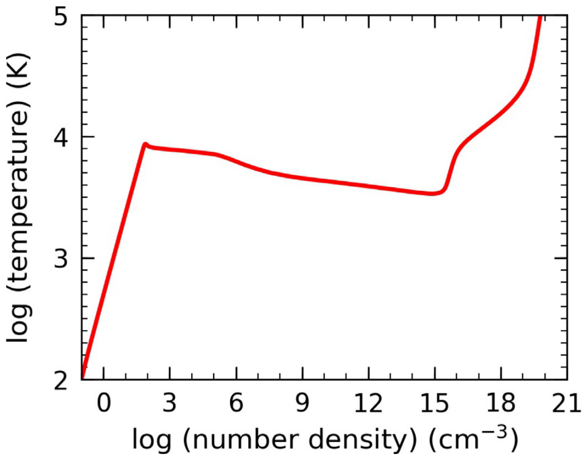

Figure B1. Temperature evolution in an one-zone calculation of gravitationally collapsing core. The horizontal axis is the number density and the vertical axis is the gas temperature.

This paper has been typeset from a TEX/LATEX file prepared by the author.